

3D Hierarchical V and N-codoped MoS₂/rGO Composite as a Potential Electrode Material Towards Hydrogen Evolution Reaction in Acidic and Alkaline pH



Saikat Bolar, Subhasis Shit, Naresh Chandra Murmu, and Tapas Kuila

1 Introduction

Hydrogen energy is becoming a contemporary sustainable and renewable resource that can overcome the global energy crisis. High energy density (120 kJ mol^{-1}) and zero carbon emissions are the main driving factors for creating the interest on hydrogen production globally [1, 2]. Currently, hydrogen is mostly produced coal gasification technique which is not an environment friendly approach [3]. Therefore, hydrogen production by water electrolysis is attracting more attention globally. However, ~5% of the total hydrogen is produced by electrolysis. The use of potential electrocatalysts has a significant impact on water electrolysis [4]. The volcano plot suggests Pt as a promising electrode material for hydrogen evolution reaction (HER) through water electrolysis [1–5]. The low efficiency, slow kinetics, high overpotential, good durability, and high cost of electrocatalysts limit sustainable hydrogen production. In order to mitigate these issues, it is necessary to design low-cost, high-efficiency, durable, and selective electrocatalysts [6–12]. Recently, 2D molybdenum

Supplementary Information The online version contains supplementary material available at https://doi.org/10.1007/978-981-19-2572-6_12.

S. Bolar · S. Shit · N. C. Murmu · T. Kuila (✉)
Surface Engineering and Tribology Division, Council of Scientific and Industrial Research—Central Mechanical Engineering Research Institute, Durgapur 713209, India
e-mail: tkuila@gmail.com

S. Bolar
e-mail: saikat.bolar@gmail.com

S. Shit
e-mail: subhasis09021994@gmail.com

N. C. Murmu
e-mail: ncmurmu@gmail.com

Academy of Scientific and Innovative Research (AcSIR), Ghaziabad 201002, India

disulphide (MoS_2) has gained attention in electrochemistry owing to the layered structure. The D-band electronic structure of MoS_2 is analogous with Pt. Therefore, MoS_2 has received extensive attention as the HER electrocatalyst [2]. However, high resistivity, poor surface active sites, unused crystal faces, and limited operational stability limit the wide applications of MoS_2 as a HER catalyst [2–5]. In this regard, it is necessary to overcome the limitation related to MoS_2 . Doping is an emerging technique that improves the electrocatalytic activity by changing the crystal structure. Therefore, doping engineering is an emerging technology that can trigger the inert basal plane of 2D MoS_2 through the creation of strain and vacancies engineering [2, 5, 13–17]. However, in some cases, doping may form defects inside the crystal structure and improve the catalytic performance [2, 7, 9]. On contrary, in harsh electrolyte media, aerial oxidation, and low operating stability reduce the wide applicability of MoS_2 or MoS_2 -supported electrocatalysts. Recently, carbon-containing materials have received considerable attention in catalyst synthesis due to the improvement in catalytic stability and electronic modification during composite formation [18]. Retention in harsh electrolytic media, high natural abundance, and huge structural robustness are considered as the significant advantages of carbonaceous materials as electrode material. Previous studies have shown that CVD-grown graphene and reduced graphene oxide have poor electrolytic performance in HER [7–15]. Most importantly, the high geometric surface area, outstanding electrical conductivity, excellent thermal stability, and tremendous mechanical strength of graphene encourage the researchers to investigate its effect on the catalytic performance of HER [7, 10, 18]. The synergistic effect within the composite structure has gained tremendous attention due to the improvement of catalytic performance. In this context, there is an urgent need to develop nanostructured composite materials to promote HER and receive great attention under different pH environment. Herein, a defect-rich V and N co-doped MoS_2 embedded in reduced graphene oxide (rGO) to prepare VNMSG composite by in situ hydrothermal technique. V and N doping appreciably modified the electronic structure of MoS_2 as reflected in the electrochemical analysis. The conductive rGO nanosheets improve the catalytic performance of VNMSG by decreasing the resistivity, catalytic stability, and activating the inert basal plane. The synergistic effect between MoS_2 and rGO nanosheets enhances the electrocatalytic performance in VNMSG.

2 Experimental Section

2.1 Material

All chemicals including, graphite powder ($\geq 99.5\%$, Sigma Aldrich), sulphuric acid (H_2SO_4 , $\geq 95\text{--}98\%$, Merck, India), nitric acid (Merck, India), potassium permanganate (KMnO_4 , (Merck, India), hydrogen peroxide (H_2O_2 , Merck, India), sodium meta vanadate (NaVO_3 , Sigma Aldrich), thioacetamide ($\text{CS}(\text{NH}_2)_2$, Sigma Aldrich),

ammonia (33%, Merck), sodium dodecyl sulphate (SDS, SRL, India), sodium molybdate dihydrate (Na₂MoO₄·2H₂O, SRL, India), ethanol (98%, Himedia), and hydrochloric acid (HCl, 30%, Merck, India) were applied without further purification.

2.2 Synthesis of V and N Co-Doped MoS₂ (VNMS)

Vanadium and nitrogen were synthetically doped in MoS₂ by one-pot solvothermal method. Typically, requisite amount of precursors were taken in a beaker and stirred vigorously in 1:1 ethanol–water mixture for ~30 min. SDS was added (greater than CMC value) as a surfactant in the solution. The mixture of solution is kept inside the hydrothermal reactor for 18 h at 180 °C. A black-coloured product was obtained after filtration which again dried at 60 °C under vacuum oven. The resultant product was dispersed in 40 ml of water-ethanol (1:1) mixture-Solution A.

2.3 Synthesis of V and N Co-Doped MoS₂/rGO (VNMSG)

Graphene oxide (GO) was synthesized as illustrated in our previous report [19]. The two solutions (solution A and B) were mixed in a 1 L flask by drop-wise addition of continuous stirring for 2 h. The resultant solutions were transferred into Teflon lined hydrothermal reactor and kept for 8 h at 120 °C. A black-coloured product was obtained by filtration and successive drying method.

2.4 Physicochemical Analysis

X-ray diffraction (XRD) patterns of the electrocatalyst were recorded with D2 PHASER, Bruker, Germany using Cu K α radiation ($\lambda = 0.15418$ nm). Raman spectra of the electrocatalysts were performed in a 100 nm sample spot size at a constant laser wavelength of 532 nm using Witec alpha 300 R. Field emission scanning electron microscopy (FE-SEM) image was collected from Σ igma HD, Carl Zeiss, Germany. High-resolution transmission electron microscopy (HR-TEM) images were recorded with JEM 2100 h-TEM (Make JEOL, Japan). X-ray photoelectron spectroscopy (XPS) was carried out with Thermo Shimadzu ESCA 3400 by monochromatic X-ray source.

2.5 Electrode Fabrication

Catalytic ink was composed of ~5 mg of electrode material and 5 mL of stock solution (contain ~100% ethanol and 0.4 volume percentage of Nafion[®], 10 wt percentage of carbon black, and DI water) in an ultrasonic bath sonicator for 45 min. Thereafter, the catalytic ink was deposited over the graphite rod electrode with a catalytic loading of 0.5 mg cm⁻² having diameter 6 mm which again dried under room temperature at around 298 K. The electrochemical analysis was performed at 298 K using potentiostat/galvanometer (PARSTATE 4000) at 1 M KOH (pH ~ 13) and 0.5 M H₂SO₄ (pH ~ 1) electrolyte, respectively. The carbon rod electrode and Ag/AgCl electrode (saturated KCl solution) were used as the counter electrode and reference electrode, respectively.

All the electrochemical data were converted into the reversible hydrogen electrode (RHE) scale by using the following electrochemical equation: [2, 5]

$$E_{\text{RHE}} = E_{\text{Ag/AgCl/Sat.KCl}} + 0.059\text{pH} + 0.197 \quad (1)$$

A number of voltammetric cycles were collected at 100 mVs⁻¹ scan rate prior to record the LSV plot. The current densities values were obtained by dividing the current response value with the geometric area of the working electrode. The linear scan voltammetry (LSV) was performed at low scan rate of 5 m Vs⁻¹ to avoid electric double-layer charging current. The series/uncompensated resistance is eliminated by iR correction method. The Tafel slope value is acquired from the Tafel equation (2). [2, 5]

$$\eta = a + b \log j \quad (2)$$

The electrochemical parameters like η , j , and b represent the overpotential, current density, and Tafel slope, respectively. For HER, the overpotential (η) was obtained by subtracting potential from zero ($\eta = 0 - E_{\text{RHE}}$) [2, 5, 20].

The electrochemical active surface area (ECSA) and the roughness factor (RF) were calculated from the non-faradic capacitive current related to electrochemical double-layer capacitance (C_{dl}) values collected from the following equations [2, 5, 20]:

$$\text{ECSA} = \frac{C_{\text{dl}}}{C_s} \quad (3)$$

$$\text{RF} = \frac{\text{ECSA}}{\text{Geometric Area of Electrode}} \quad (4)$$

C_s is the specific capacitance of an automatically smooth planer surface of the working electrode. The area normalized specific capacitance was found to be 40 and 35 μFcm^{-2} in 1 M KOH and 0.5 M H₂SO₄, respectively [2, 5, 20, 21]. The C_s value of the electrocatalyst was measured from the multiple CV curves within a

specific potential window at different scan rates (ν). The specific capacitance values of the electrocatalyst were ascribed from Δj versus ν plot where Δj values were obtained from half of the difference between the anodic and cathodic current density (j_a and j_b).

$$\Delta j = (j_a - j_b)/2 \quad (5)$$

The chronoamperometric study was carried out at a fixed working potential to understand the long-term permanence of the electrocatalyst at different electrolyte (acidic and alkaline) medium. Electrochemical impedance spectroscopy (EIS) was performed within 10⁵ to 0.1 Hz frequency range to investigate the dynamics related with the electrochemical changes that occur during the HER process at the electrode and electrolyte interface. Nyquist plot was performed after EIS analysis, and the Randles equivalent circuit model was fitted by using Z view[®] software (Scribner Associates Inc. USA).

3 Result and Discussion

3.1 Physicochemical Analysis

The crystal structure of the electrocatalyst was investigated by XRD analysis (Fig. 1). The XRD pattern of GO consisted of (001) and (100) crystal planes (Fig. 1a). The appearance of (100) diffraction peak indicated that the surface of GO was not fully interconnected with the oxygen functionalities [22]. The chemical reduction of GO in VNMSG was confirmed by the appearance of a broad (002) peak at $2\theta \approx 24^\circ$ (Fig. 1b, f). The wide (002) diffraction peak suggest that the reduced GO (rGO) was amorphous in nature as confirmed by the HR-TEM and FE-SEM image analysis (Fig. 1f). The diffraction patterns of VNMSG at $2\theta \approx 14.05, 33.50, 39.82,$ and 58.52° were ascribed as the (002), (100), (103), and (110) lattice planes of hexagonal MoS₂ crystal structure as demonstrated in Fig. 1b, c [2, 5]. Therefore, the XRD pattern of VNMSG matched well with the JCPDS card no #77-1716. A small shift in (002) peak position of VNMSG can be ascribed by the negligible change in lattice parameters on V and N co-doping in MoS₂ (Fig. 1d, e) [2, 5, 18]. Thiourea acting as the sulphide source of MoS₂ and reducing agent for GO to rGO conversion by H₂S formation during the solvothermal method. The broad diffraction peak of rGO in composite structure is attributed to the formation of stacked rGO sheets [23]. These observations suggested that the rGO nanosheets controlled nucleation and subsequent growth of MoS₂ over the conducting scaffold.

The existence of rGO in the VNMSG was investigated with Raman spectroscopy as depicted in Fig. 2a–c. Two characteristic peaks of hexagonal MoS₂ appeared at ~ 410 and 380 cm^{-1} in both MoS₂ and VNMSG composite belong to A_{1g} (out of plane vibration of S atom) and E¹_{2g} (in-plane Mo–S phonon mode) Raman modes

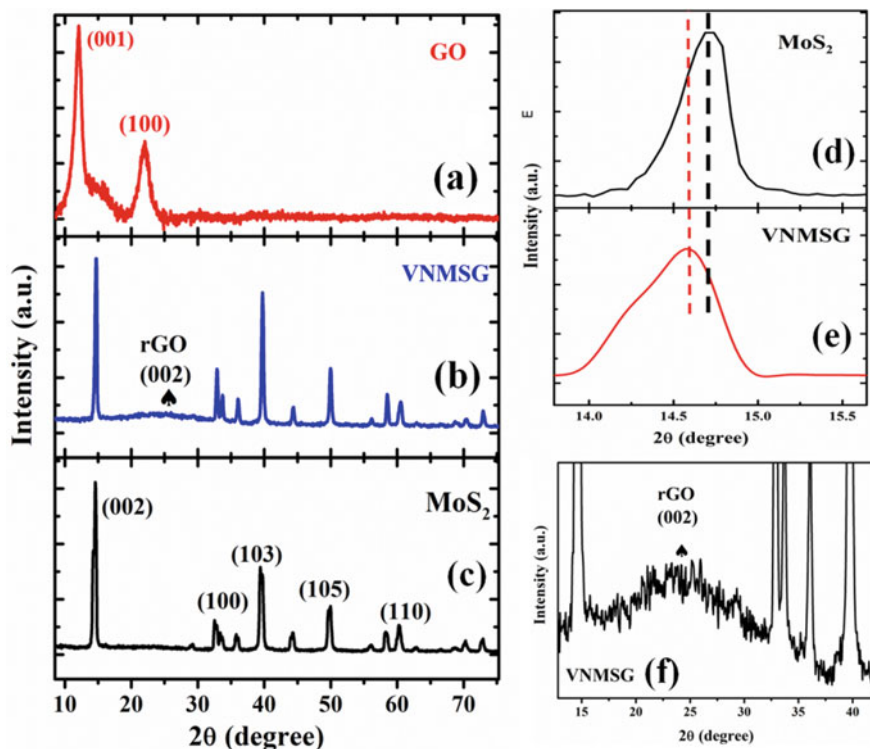


Fig. 1 a–c XRD pattern of graphene oxide, VNMSG, MoS₂; d, e (002) peak position of MoS₂ and VNMSG; f (002) crystal plane of VNMSG

(Fig. 2a, f) [2, 5, 18]. V and N co-doping in MoS₂ hardly reveal any additional peak in the Raman spectra conforming the successful formation of doped MoS₂. The shift in Raman modes (A_{1g} and E^{1}_{2g}) in VNMSG compared to pure MoS₂ confirmed the formation of lattice distortion due to the V and N dual doping in MoS₂ [2]. The lattice mismatch in VNMSG is observed due to the formation of V–S and Mo–N bonds in the MoS₂ crystal structure leading to the formation of stress in the VNMSG composite. In addition, the peak at $\sim 1350\text{ cm}^{-1}$ (random agreement of graphite crystallites) is called the D-band and at $\sim 1580\text{ cm}^{-1}$ (stretching vibration of sp^2 hybridized C atoms) called the G-band appeared in VNMSG and GO as shown in Fig. 2d, e [22, 23]. A gradual increase in intensity of the D to G-band ratio (I_D/I_G) in GO (value: 0.72) and VNMSG (value: 0.92) as shown in Fig. 2g. The higher I_D/I_G ratio confirmed that more sp^2 domains were formed indicating the defect structure of rGO in VNMSG (Fig. 2g). It is speculated that the catalytic performance of VNMSG was significantly improved with increasing the defect.

XPS was used to examine the surface structure, chemical state, and electronic interaction in the VNMSG composite. XPS survey spectra analysis confirmed that V and N atoms were successfully doped in the MoS₂ crystal lattice (Fig. S1). The atomic

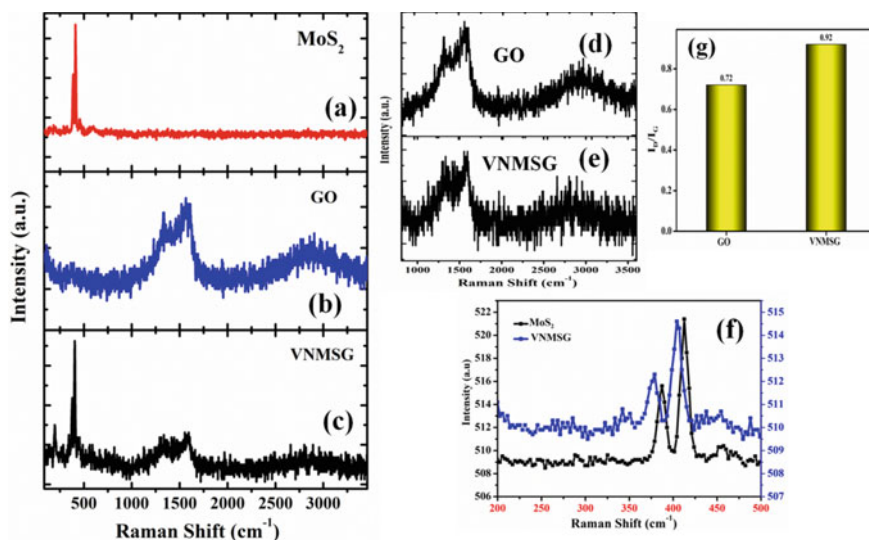


Fig. 2 a–c Raman spectra of MoS₂, GO, and VNMSG; **d, e** Raman spectra at selected region of GO and VNMSG; **f** Raman spectra at selected region of MoS₂ and VNMSG; **g** calculated I_D/I_G ratio of GO and VNMSG

percentage ratio of Mo and S implied that MoS₂ was formed in the VNMSG during the solvothermal synthetic process. The V doping percentage in MoS₂ was higher compared to the N, which can be attributed to the size of the dopant, the particular reaction conditions, and the source of the dopant. XRD and Raman spectra suggested that GO controlled the growth of MoS₂ which is reflected in Mo3d XPS spectra (Fig. 3b). The deconvoluted XPS spectrum of Mo3d of VNMSG was composed of four characteristic peaks. Two intense peaks of Mo 3d_{5/2} (229.5 eV) and Mo 3d_{3/2} (232.7 eV) suggested the presence of MoS₂ in VNMSG while peak of Mo 3d (235.9 eV) at high binding energy corresponds to MoO₃ or MoO₄²⁻ formation during the solvothermal synthesis method (Fig. 3b) [2, 13, 15]. Due to the successful formation of composite structure, the small shift of the Mo3d peak position indicated the electron transfer phenomenon. Mo⁶⁺ oxidation state appeared due to the partial oxidation of Mo atoms at MoS₂ edges and defects formation in the MoS₂ crystal lattice during the composite structure formation. This occurrence implied the formation of a synergistic effect in VNMSG indicating the better catalytic efficiency. The deconvoluted S2p_{1/2} and S2p_{3/2} peaks at 162.70 and 163.92 eV for VNMSG appeared at relatively higher binding energy region than pure MoS₂ indicating the successful formation of the nanocomposite with rGO (Fig. 3c) [2, 24]. A small peak located at ~168.1 eV belongs to the oxidized sulphur which may be due to the composite structure formation. The low intensity of two doublet peaks at ~524.44 and 517.01 eV of V2p spectra in VNMSG suggested that V was successfully doped in VNMSG as shown in Fig. 3d [5]. The S/Mo total area ratio was calculated from the fitted S 2p and Mo 3d core-level spectra of MoS₂ and VNMSG (Fig. 3f). The

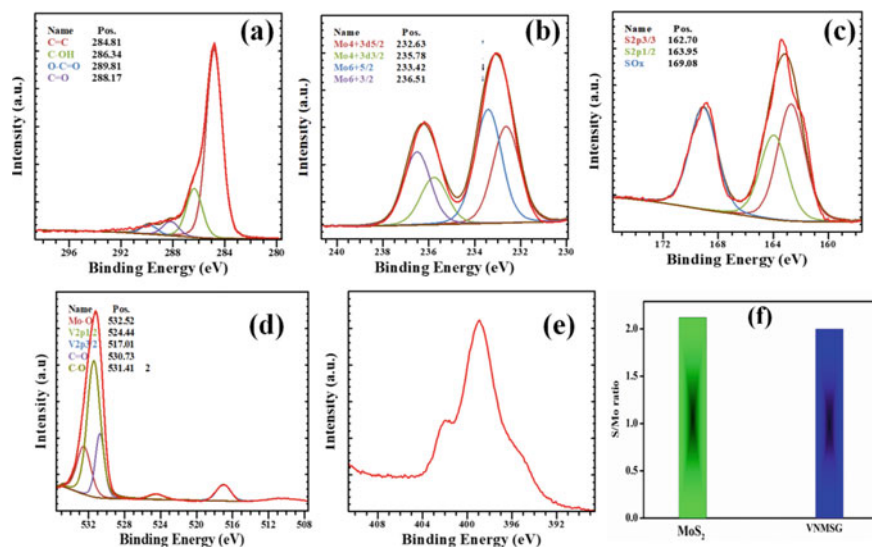


Fig. 3 Deconvoluted XPS data of C1s (a), Mo3d (b), S2p (c), V2p (d), and N1s (e), respectively

S/Mo ratio of VNMSG was lower than pure MoS₂ which suggested a creation of S vacancies in the VNMSG on doping. It is well evident that S vacancies improved the HER performance by activation of active basal plane and defect formation at edge sites of MoS₂. The shifts in deconvoluted V2p XPS spectra towards higher binding energy in composite can be attributed to the presence of electronic interaction between V-doped MoS₂ and rGO conducting scaffold [5, 25]. The intensity of V2p peak was lower than the O1s XPS spectra. Interestingly, the deconvoluted O1s spectra composed of characteristic peak of M–O, C=O, and C–O bond as present in VNMSG composite structure (Fig. 3d, S2). Figure 3e shows the presence of N 1s in VNMSG and the absence of C–N bond in the deconvoluted XPS spectra of C1s implied that MoS₂ was doped with N. Therefore, nitrogen-doped rGO was not formed in the solvothermal method. The deconvoluted C1s spectra of VNMSG represented the presence of non-oxygenated C–C double bond along with other functional groups like C–C/C–H, C=O/O–C–O in rGO nanosheets in VNMSG (Fig. 3a) [23–26].

Morphological study showed that MoS₂ nanoflower was grafted over the rGO nanosheets. The rGO nanosheets present as a conducting template and controlled the growth of MoS₂ (Fig. 4a, b). The MoS₂ nanosheets were embedded on the rGO sheets through interfacial van der Waals interaction. TEM image of VNMSG showed a homogenous growth of MoS₂ over the conducting rGO scaffold that enhanced the overall active surface area of the electrocatalyst and reduced the agglomeration possibilities of MoS₂ (Fig. 4d). It is also assumed that the interfacial interaction between the doped MoS₂ and rGO sheets definitely modified the electronic structure and band alignment of the composite structure; thereby, electrochemical performance of the VNMSG composite was modified significantly. The IFFT pattern in R1 region

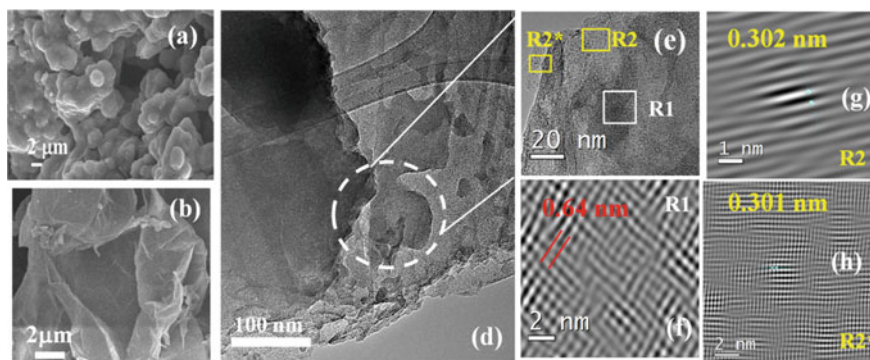


Fig. 4 FESEM image of **a** VNMSG, **b** GO; **d** TEM image of VNMSG, **e** HR-TEM image of VNMSG, **f** IFFT pattern of R1 represent (002) crystal plane of MoS₂; **g**, **h** IFFT pattern of R2 and R2* represent (002) plane of rGO nanosheets

indicates the presence of (002) crystal plane of MoS₂ in VNMSG composite (Fig. 4e, f) [2, 5, 13, 15]. The (002) crystal plane of rGO appeared in R2 and R2* regions implying the successful formation of the composite structure (Fig. 4g, h) [25, 26]. HR-TEM image analysis recommended a strong interfacial interaction present within the rGO nanosheets and MoS₂ which confirmed the existence of synergistic interaction in VNMSG nanocomposite. The HR-TEM image failed to confirm the formation of defect region within the composite structure. However, Raman and XPS analysis suggest the formation of defect-rich composite structure.

3.2 Electrochemical Analysis

The HER activity of the developed electrocatalyst was analysed in acidic and alkaline electrolyte. The polarization curves demonstrated that the catalytic performance of pure MoS₂ was improved upon doping and heterostructure formation. Figure 5a & 6a suggested that VNMSG had lowest overpotential value than the other electrode materials. VNMSG required ~ 88 and 132 mV overpotential to attain 10 mAcm⁻² current density [27, 28]. It is well established that the HER activity of an electrocatalyst was more facile in acidic electrolyte than in alkaline electrolyte as confirmed by the polarization curve (Table 1–2). The order of electrochemical performance depends on the electronic and structural modification of MoS₂ during synthesis. The enhanced electrochemical performance of VNMSG can be attributed to the synergistic interaction within the rGO nanosheets and MoS₂. However, the doping inside the MoS₂ has a potential impact on the electronic modification and improved catalytic activity. The adsorption–desorption performance of the electrocatalyst was augmented significantly upon doping inside the MoS₂ and composite structure formation with the rGO sheets. The enhanced adsorption–desorption ability of VNMSG can be attributed to

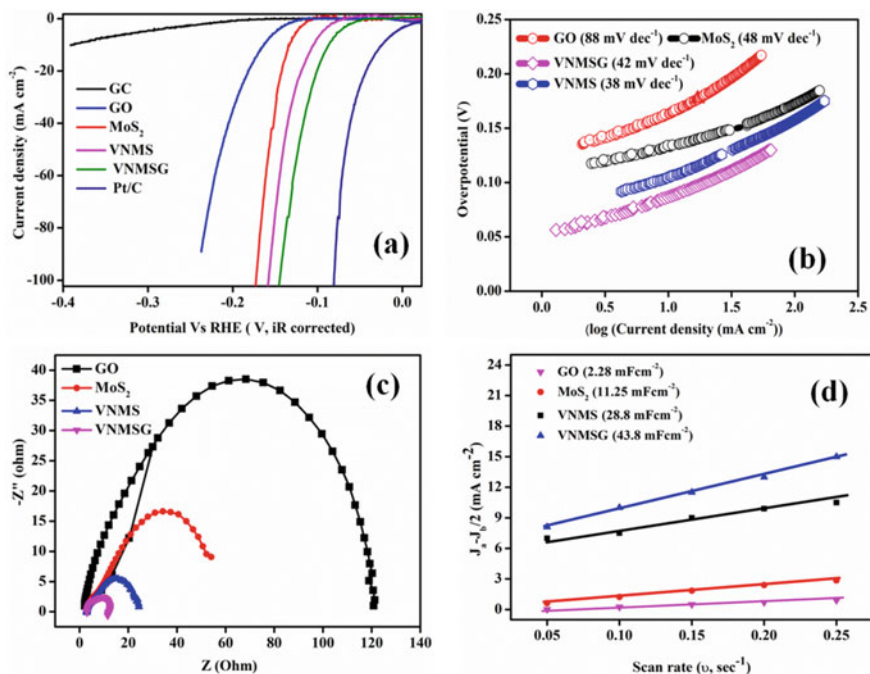


Fig. 5 a LSV plot; b Tafel slope; c EIS plot d ECSA of the electro catalysts (electrochemical tests were carried out in 0.5 M H₂SO₄ medium)

Table 1 Electrochemical performance for HER in acidic medium

Material	Electrolyte medium	Overpotential @ 10 mA cm ⁻² current density	Tafel slope (mV dec ⁻¹)	Exchange current density (mAcm ⁻²)
GO	Acidic	163	88	3.02×10^{-2}
MoS ₂	Acidic	134	48	6.5×10^{-2}
VNMS	Acidic	106	42	6.3×10^{-2}
VNMSG	Acidic	89	38	9.5×10^{-2}

Table 2 Electrochemical performance for HER in alkaline medium

Material	Electrolyte medium	Overpotential @ 10 mA cm ⁻² current density	Tafel slope (mV dec ⁻¹)
GO	Alkaline	191	208
MoS ₂	Alkaline	146	145
VNMS	Alkaline	139	142
VNMSG	Alkaline	133	92

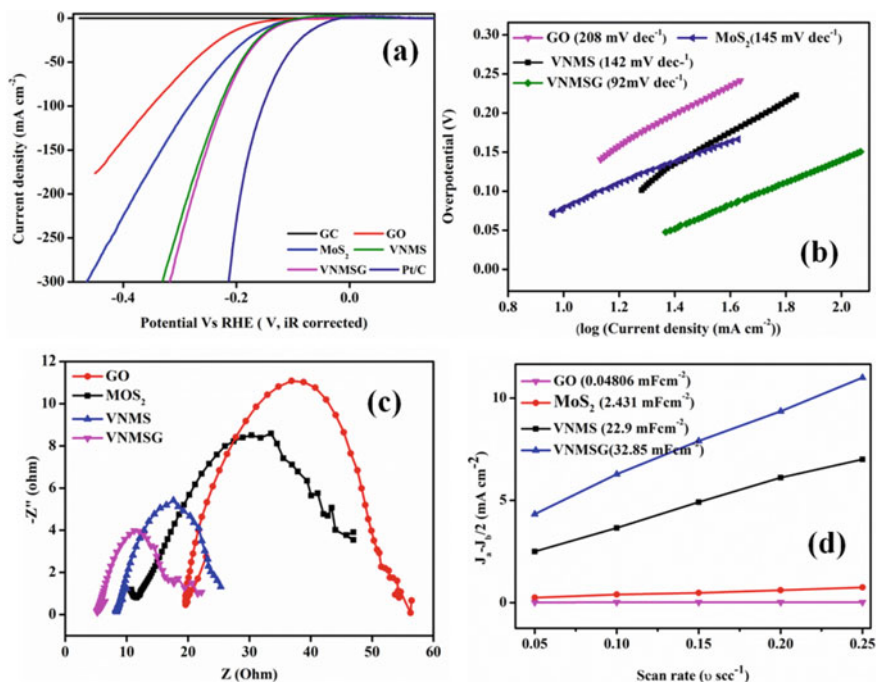


Fig. 6 a LSV plot; b Tafel slope; c EIS plot, d ECSA of the electrocatalysts (electrochemical tests were carried out in 1 M KOH medium)

the exposed surface active sites. The rGO nanosheets assisted to graft the MoS₂ nanopetals on its surface; thereby, the effective active surface area of the VNMSG was increased. The ECSA (Figs. 5d and 6d) values calculated from the CV plots (Figs. S3 and S4) confirmed the improvement in surface adsorption performance upon composite formation. In addition, V and N co-doping in MoS₂ lattice structure developed defects, thereby more exposed active sites were formed (Tables S4 and S5).

Tafel slope is considered as leading parameters in HER which signify the potential require enhancing the current response by an order of 10 times than the initial. Therefore, a low Tafel slope suggests a faster HER kinetics implies a better catalytic ability. Tafel plots were acquired from the linear region of the LSV plot as depicted in Figs. 5b and 6b. Interestingly, the Tafel slope values of the developed electrocatalyst were calculated from the linear region from Tafel equation ($\eta = b \log j + a$, where b = Tafel slope, j = current density). The Tafel slope value for VNMSG composite was smallest among other electrocatalyst in acidic and alkaline pH (Tables S1 and S2). The lowest Tafel slope value of VNMSG suggested a better catalytic performance. Above all the small Tafel slope of VNMSG nanohybrid was beneficial for catalytic application as it leads to a rapid increase in HER rate with the change in overpotential. The HER process includes Volmer step, Heyrovsky step, and Tafel steps, respectively.

The Volmer step allied with proton absorption is suggesting the rate-limiting step with a slope of $\sim 120 \text{ mVdec}^{-1}$ while Heyrovsky and Tafel steps should recommend ~ 40 and $\sim 30 \text{ mVdec}^{-1}$ slope value to be a rate-limiting one [2, 5, 20, 29, 30]. Therefore, Tafel slope values of the synthesized electrocatalyst suggested a Volmer–Heyrovsky reaction mechanism. However, the electrochemical adsorption and desorption was considered as the rate-limiting step in both alkaline and acidic pH, respectively. The low Tafel slope values of VNMSG were recognized by the strong electronic coupling appeared due to interfacial interaction with the rGO nanosheets and V, N-codoped MoS_2 . The charge transfer resistance (R_{ct}) values of the electrocatalyst supported the catalytic order in both acidic and alkaline medium (Figs. 5c and 6c) [31]. The improved R_{ct} values can be ascribed as the combination effect of doping in MoS_2 and composite structure formation (Figs. S5 and S6). The synergistic effect developed in VNMSG increased the charge carrier density of VNMSG thereby the H adsorption–desorption process is getting augmented as reflected in the polarization plot [29]. The improved charge carried density of VNMSG was found as the highly conducting rGO nanosheets attached with the MoS_2 nanoflower, thereby the overall R_{ct} resistance is decreased (Tables S5 and S6).

The electrocatalytic durability of the synthesized conducting scaffold supported doped MoS_2 composite was checked by polarization plot before and after the 1000 CV in the acidic and alkaline medium at a fixed scan rate of 10 mVs^{-1} . The polarization curves matched closely with the initial one with a negligible change in current response at fixed overpotential (depicted in Fig. 7a, b). The chronoamperometry study was prolonged at the current density of 55 mAcm^{-2} and 15 mAcm^{-2} for ~ 7 h in acidic and ~ 8 h for alkaline pH, respectively. A negligible change in potential demonstrated a negligible change in electrochemical performance (depicted in Fig. 7c, d).

4 Conclusions

In summary, V and N co-doped MoS_2 nanopetals embedded on rGO a nanosheet was developed by a facile solvothermal synthetic method. The defect-rich VNMSG nanocomposite exhibited enhanced catalytic activity and remarkable structural stability in acidic and alkaline electrolyte. Physicochemical analysis suggested the successful formation of doped composites. In addition, V and N doping in MoS_2 modified the electronic structure, thereby raising the valence band structure of the doped nanocomposite to the Fermi level. HR-TEM and XPS analysis confirmed the strong interfacial interaction between rGO nanosheets and MoS_2 nanopetals. Therefore, the participation of rGO nanosheets improved the overall conductivity of the composite, thereby promoting the HER process. The excellent HER performance was attributed to the large number of active surface sites, which can be ascribed by the high active site density and relatively large exposed surface area. The participation of rGO nanosheets significantly improved the catalytic durability in acidic and alkaline media. Most importantly, the synergistic action between rGO nanosheets and MoS_2 nanopetals facilitated to enhance the HER performance of VNMSG composites.

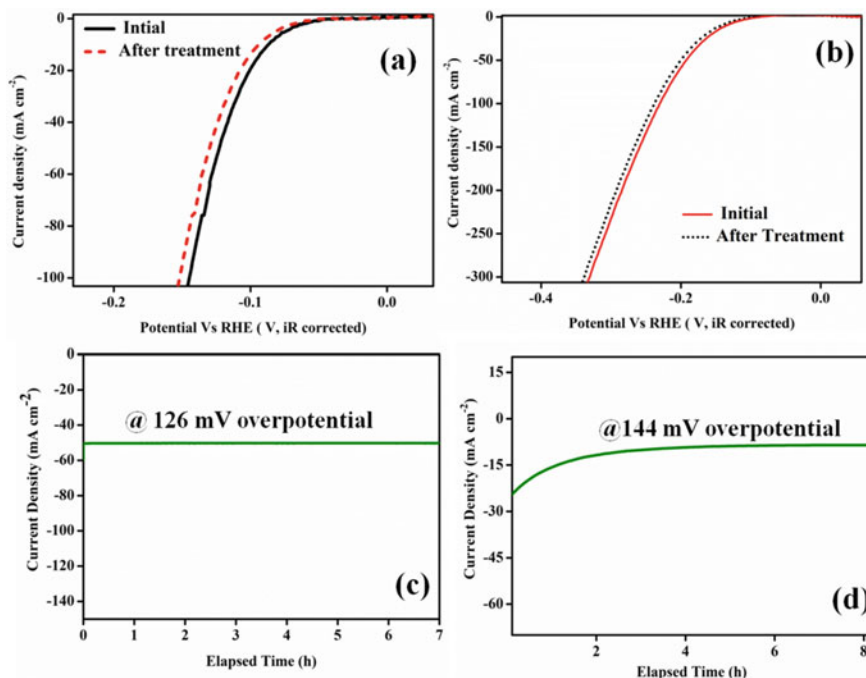


Fig. 7 **a, b** LSV plot of VNMSG before and after 1000 cycle at a scan rate of 10 mVs^{-1} in $0.5 \text{ M H}_2\text{SO}_4$ and 1 M KOH , respectively. **b** Chronoamperometric study in $0.5 \text{ M H}_2\text{SO}_4$ of VNMSG at 126 mV overpotential for $\sim 7 \text{ h}$, **d** chronoamperometric study in 1 M KOH of VNMSG at 144 mV overpotential for $\sim 8 \text{ h}$

Acknowledgements The authors would like to thank the Defence Research and Development Organization of India (DRDO) for financial and instrumental facilities, project number GAP-219012. The authors also thank CSIR-CMERI, Durgapur.

References

1. Chu S, Majumdar A (2012) Opportunities and challenges for a sustainable energy future. *Nature* 488:294–303
2. Bolar S, Shit S, Murmu NC, Samanta P, Kuil T (2021) Activation strategy of MoS₂ as HER electrocatalyst through doping-induced lattice strain, band gap engineering, and active crystal plane design. *ACS Appl Mater Interfaces* 13:765–780
3. El-Emam RS, Ozcan H (2019) Comprehensive review on the techno-economics of sustainable large-scale clean hydrogen production. *J Clean Prod* 220:593–609
4. Zhao G, Rui K, Dou SX, Sun W (2018) Heterostructures for electrochemical hydrogen evolution reaction: a review. *Adv Funct Mater* 28:1803291
5. Bolar S, Shit S, Kumar S, Murmu NC, Ganesh S, Inokawa H, Kuila T (2019) Optimization of active surface area of flower like MoS₂ using V-doping towards enhanced hydrogen evolution reaction in acidic and basic medium. *Appl Cat B* 25:432–442

6. Guo Y, Park T, Yi JW, Henzie J, Kim J, Wang Z, Jiang B, Bando Y, Sugahara Y, Tang J, Yamauchi Y (2019) Nano architectonics for transition metal sulfide-based electrocatalysts for water splitting. *Adv Mater* 31:1807134
7. Wu Z, Song M, Zhang Z, Wang J, Wang H, Liu X (2019) Porous two dimensional layered molybdenum compounds coupled with N-doped carbon based electrocatalysts for hydrogen evolution reaction. *Appl Surf Sci* 465:724–729
8. Sun H, Yan Z, Liu F, Xu W, Cheng F, Chen J (2020) Self-supported transition-metal-based electrocatalysts for hydrogen and oxygen evolution. *Adv Mater* 32:1806326
9. Chandrasekaran S, Yao L, Deng L, Bowen C, Zhang Y, Chen S, Lin Z, Peng F, Zhang P (2019) Recent advances in metal sulfides: from controlled fabrication to electrocatalytic, photocatalytic and photoelectrochemical water splitting and beyond. *Chem Soc Rev* 48:4178–4280
10. Noor S, Sajjad S, Leghari SAK, Flox C, Kallio T (2020) Efficient electrochemical hydrogen evolution reaction and solar activity via bi-functional GO/Co₃O₄-TiO₂ nano hybrid structure. *Int J Hydrogen Energy* 45:17410–17421
11. Eftekhari A (2017) Electrocatalysts for hydrogen evolution reaction. *Int J Hydrogen Energy* 42:11053–11077
12. Zhang X, Du Z, Luo X, Sun A, Wu Z, Wang D (2018) Template-free fabrication of hierarchical MoS₂/MoO₂ nanostructures as efficient catalysts for hydrogen production. *Appl Surf Sci* 433:723–729
13. Luo Z, Ge J, Liu C, Xing W (2020) Engineering the HER catalytic behavior of heteroatom-doped molybdenum disulfide via versatile partial cation exchange. *J Energy Chem* 41:15–19
14. Wei C, Wu W, Li H, Lin X, Wu T, Zhang Y, Xu Q, Zhang L, Zhu Y, Yang X, Liu Z, Xu Q (2019) Atomic plane-vacancy engineering of transition-metal dichalcogenides with enhanced hydrogen evolution capability. *ACS Appl Mater Interfaces* 11:25264–25270
15. Wang D, Zhang X, Bao S, Zhang Z, Fei H, Wu Z (2017) Phase engineering of a multiphase 1T/2H MoS₂ catalyst for highly efficient hydrogen evolution. *J Mater Chem A* 5:2681–2688
16. Linghu Y, Wu C (2020) Strain engineering the behaviors of small molecules over defective MoS₂ monolayers in the 2H and 1T0 phases. *J Mater Sci* 55:10643–10655
17. Zhao M, Ma X, Yan S, Xiao H, Li Y, Hu T, Zheng Z, Jia J, Wu H (2020) Solvothermal synthesis of oxygen-incorporated MoS_{2-x} nanosheets with abundant under coordinated Mo for efficient hydrogen evolution. *Int J Hydrogen Energy* 45:19133–19143
18. Dong W, Liu H, Liu X, Wang H, Li X, Tian L (2021) Defective-MoS₂/rGO heterostructures with conductive 1T phase MoS₂ for efficient hydrogen evolution reaction. *Int J Hydrogen Energy* 46:9360–9370
19. Ghosh S, Samanta P, Samanta P, Murmu NC, Kuila T (2020) Investigation of electrochemical charge storage efficiency of NiCo₂Se₄/RGO composites derived at varied duration and its asymmetric supercapacitor device. *Energy Fuels* 34:13056–13066
20. Bolar S, Shit S, Murmu NC, Kuila T (2020) Doping-assisted phase changing effect on MoS₂ towards hydrogen evolution reaction in acidic and alkaline pH. *ChemElectroChem* 7:336–346
21. McCrory CCL, Jung S, Peters JC, Jaramillo TF (2015) Benchmarking hydrogen evolving reaction and oxygen evolving reaction electrocatalysts for solar water splitting devices. *J Am Chem Soc* 137(13):4347–4357
22. Kuila T, Bhadra S, Yao D, Kim NH, Bose S, Lee JH (2010) Recent advances in graphene based polymer composites. *Prog Polym Sci* 35:1350–1375
23. Smith AT, LA Chance AM, Zeng S, Liu B, Sun L (2019) Synthesis, properties, and applications of graphene oxide/reduced graphene oxide and their nanocomposites. *Nano Mater Sci* 1:31–47
24. Lu X, Lin Y, Dong H, Dai W, Chen X, Qu X, Zhang X (2017) One-step hydrothermal fabrication of three-dimensional MoS₂ nanoflower using polypyrrole as template for efficient hydrogen evolution reaction. *Sci Rep* 7:42309
25. Kuila T, Mishra AK, Khanra P, Kim NH, Lee JH (2013) Recent advances in the efficient reduction of graphene oxide and its application as energy storage electrode materials. *Nanoscale* 5:52–71
26. Dreyer DR, Park S, Bielawski CW, Ruoff RS (2010) The chemistry of graphene oxide. *Chem Soc Rev* 39:228–240

27. Li C, Baek JB (2020) Recent advances in noble metal (Pt, Ru, and Ir)-based electrocatalysts for efficient hydrogen evolution reaction. *ACS Omega* 5(1):31–40
28. Li Z, Ge R, Su J, Chen L (2020) Recent progress in low Pt content electrocatalysts for hydrogen evolution reaction. *Adv Mater Interface* 7(14):2000396
29. Shinagawa T, Esparza ATG, Takanabe K (2015) Insight on Tafel slopes from a microkinetic analysis of aqueous electrocatalysis for energy conversion. *Sci Rep* 5:13801
30. Bolar S, Shit S, Murmu NC, Kuila T (2020) FeNiS_x@MoS₂ heterostructure: a bioinspired nonprecious electrocatalyst for the hydrogen evolution reaction in acidic and basic media. *Chemelectrchem* 7:3324–3335
31. Wei ZW, Wang HJ, Zhang C, Xu K, Lu XL, Lu TB (2021) Reversed charge transfer and enhanced hydrogen spillover in platinum nanoclusters anchored on titanium oxide with rich oxygen vacancies boost hydrogen evolution reaction. *Angew Chem Int Ed* 60:16622–16627